ADVANCED ENERGY MATERIALS
www.advenergymat.de

Check for updates

Controlling Iron Versus Oxygen Redox in the Layered Cathode $Na_{0.67}Fe_{0.5}Mn_{0.5}O_2$: Mitigating Voltage and Capacity Fade by Mg Substitution

*Edouard Boivin, Robert A. House, John-Joseph Marie, and Peter G. Bruce**

Layered oxides for Na-ion batteries containing Fe have attracted strong interest mainly due to their low cost. However, full oxidation of Fe^{3+} to Fe^{4+} is rarely seen before O-redox sets in and is typically accompanied by voltage and capacity fade on cycling. On charging P2-$Na_{0.67}[Fe_{0.5}Mn_{0.5}]O_2$, Fe^{3+} is oxidized to only $\approx Fe^{3.3+}$ before the onset of O-redox. O-redox occurs when the Na content is sufficiently low (Na ≈0.3) to permit the transition from P-type to O-type stacking, thus enabling Fe^{3+} migration to the Na layer. Fe^{3+} migration generates cation vacancies in the transition metal layer, forming □-O-□ configurations, which trigger the onset of O-redox. In contrast, doping this material with Mg^{2+} to form P2-$Na_{0.67}[Fe_{0.25}Mn_{0.6}Mg_{0.15}]O_2$ allows full oxidation of Fe^{3+} to Fe^{4+} before the Na content is low enough to favor O-type stacking. During O-redox, Mg^{2+} is displaced into the Na layers instead of Fe. Mg substitution enables greater reversibility of the Fe^{3+}/Fe^{4+} redox couple and significantly suppresses Fe migration, which is responsible for the voltage and capacity fade observed for P2-$Na_{0.67}Fe_{0.5}Mn_{0.5}O_2$.

1. Introduction

Na-ion batteries are of interest for applications in which cost is of paramount importance.[1–4] In this regard, there is significant interest in layered oxides containing manganese and especially iron, such as P2-$Na_{0.67}[Fe_{0.5}Mn_{0.5}]O_2$ with a capacity exceeding 180 mAh g^{-1}.[5] However, such Fe-rich compounds typically do not utilize the full $Fe^{3+/4+}$ redox couple before O-redox, and they suffer from significant voltage and capacity fading.[5–11] Replacing some of the transition metal (TM) ions on the TM layers with alkali or alkali-earth cations has been shown to improve their performance.[12–20]

Here, we investigate the tie-line between $Na_{0.67}Fe_{0.5}Mn_{0.5}O_2$ and $Na_{0.67}Mn_{0.72}Mg_{0.28}O_2$ in the P2 structure-type and select the best performing composition, $Na_{0.67}[Fe_{0.25}Mn_{0.6}Mg_{0.15}]O_2$, for further study. We show that Mg substitution in this material leads to complete separation of Fe and O oxidation allowing full use of the $Fe^{3+/4+}$ redox couple, resulting in significantly improved capacity retention and reduced voltage fade compared with P2-$Na_{0.67}Fe_{0.5}Mn_{0.5}O_2$.

On charging P2-$Na_{0.67}Fe_{0.5}Mn_{0.5}O_2$, the oxidation of Fe^{3+} only reaches $\approx Fe^{3.3+}$ before enough Na has been removed from the Na layers to trigger the P2 to O2 transition. O-type stacking permits the migration of the remaining Fe^{3+} from the transition metal layer to the alkali metal (AM) layer leaving behind vacancies and forming linear □-O-□ configurations, which brings oxidation of O^{2-} within the voltage range of $Fe^{3+/4+}$. On discharge, iron is fully reduced to +3, but the migration of Fe back to the TM layer is only partially reversible. Hence, on cycling more Fe becomes trapped in the Na layer and Fe redox activity decreases, leading to a gradual voltage fade and capacity loss. In contrast, upon charging P2-$Na_{0.67}Fe_{0.25}Mn_{0.6}Mg_{0.15}O_2$, Fe^{3+} can be completely oxidized to Fe^{4+} before the Na content is sufficiently depleted to trigger a transition to O-type stacking. Then, during O-redox, Mg^{2+} (rather than Fe^{4+}) migrates into the Na layer. On discharge, Fe^{4+} is fully reduced to Fe^{3+} and Mg^{2+} almost completely returns to the TM layer. As a result, Mg substitution in P2-$Na_{0.67}Fe_{0.5}Mn_{0.5}O_2$ preserves Fe^{3+}/Fe^{4+} redox over cycling and hence inhibits the voltage fade and capacity loss.

2. Results and Discussion

2.1. Structure and Electrochemical Behavior

Materials belonging to the $Na_{0.67}Mn_{0.72}Mg_{0.28}O_2$-$Na_{0.67}Fe_{0.5}Mn_{0.5}O_2$ tie-line were synthesized as described in the methods section. Their X-Ray Powder Diffraction (XRPD) patterns are shown in Figure S1, Supporting Information. They crystallize in the P2 structure shown in **Figure 1**. However, while the Mg-rich end member of the tie-line, $Na_{0.67}Mn_{0.72}Mg_{0.28}O_2$, exhibits superstructure peaks due to the honeycomb ordering

E. Boivin,[+] R. A. House, J.-J. Marie, P. G. Bruce
Department of Materials
University of Oxford
Parks Road, Oxford, UK
E-mail: peter.bruce@materials.ox.ac.uk
P. G. Bruce
Department of Chemistry
University of Oxford
South Parks Road, Oxford, UK

The ORCID identification number(s) for the author(s) of this article can be found under https://doi.org/10.1002/aenm.202200702.

© 2022 The Authors. Advanced Energy Materials published by Wiley-VCH GmbH. This is an open access article under the terms of the Creative Commons Attribution License, which permits use, distribution and reproduction in any medium, provided the original work is properly cited.

[+]Present address: Univ. Lille, CNRS, Centrale Lille, ENSCL, Univ. Artois, UMR 8181-UCCS-Unité de Catalyse et Chimie du Solide, Lille F-59000, France

DOI: 10.1002/aenm.202200702

16146840, 2022, 30, Downloaded from https://onlinelibrary.wiley.com/doi/10.1002/aenm.202200702 by Test, Wiley Online Library on [13/10/2022]. See the Terms and Conditions (https://onlinelibrary.wiley.com/terms-and-conditions) on Wiley Online Library for rules of use; OA articles are governed by the applicable Creative Commons License

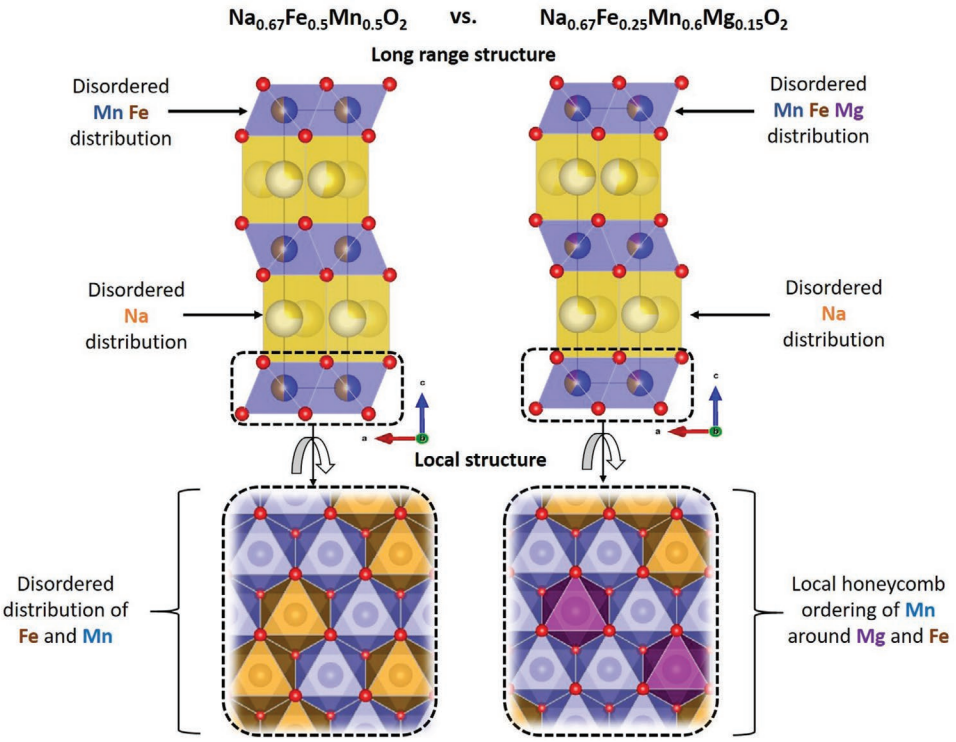


Figure 1. Long range and local structure of $Na_{0.67}Fe_{0.5}Mn_{0.5}O_2$ (left) and $Na_{0.67}Fe_{0.25}Mn_{0.6}Mg_{0.15}O_2$ (right). Purple, blue and orange octahedra represent Mg, Mn, and Fe respectively, and Na is in yellow.

of ≈6 Mn around each Mg forming a hexagonal pattern, similar to that observed in $Li[Li_{1/3}Mn_{2/3}]O_2$,[21] the peak intensities progressively decrease with increasing Fe content until they disappear completely for the $Na_{0.67}Fe_{0.25}Mn_{0.6}Mg_{0.15}O_2$ composition (see Figure S1, Supporting Information). The structures of Mg-free $Na_{0.67}Fe_{0.5}Mn_{0.5}O_2$ and Mg-substituted $Na_{0.67}Fe_{0.25}Mn_{0.6}Mg_{0.15}O_2$ were refined using XRPD and neutron powder diffraction (NPD) data, Figure S2 and Tables S1 and S2, Supporting Information. The TM cations are disordered over the long range within the TM layer, as indicated by the absence of superstructure peaks in the NPD patterns. In order to probe the local cation distribution within the TM layer, Extended X-ray absorption fine structure (EXAFS) was employed. Figure S3, Supporting Information, shows the Mn, Fe and Mg K-edges EXAFS for the two materials. The first M–O shell intensities for Fe, Mn, and Mg are similar for both materials, in accord with their coordination by 6 oxygen atoms in octahedral sites. In contrast, the second shell intensities (arising from M–M scattering) exhibit significant differences. The Mn K-edge 2nd shell intensity is significantly lower in the presence of Mg, while the Fe K-edge 2nd shell intensity shows a smaller change, indicative of Mg^{2+} being preferentially located around Mn despite the long-range disorder in the TM layer identified by diffraction. In order to further characterize the cation distribution within the TM layer, neutron pair distribution function (n-PDF) analysis was employed.

The n-PDF patterns of both materials, shown in Figure S3, Supporting Information, reveal two peaks in the 1.8–2.0 range corresponding to the negative Mn–O and the positive Mg/Fe-O scattering. As these two peaks cannot be described using the $P6_3/mmc$ space group identified by diffraction, a $Na_{2/3}Mn_{2/3}Mg_{1/3}O_2$-like honeycomb model ($P6_3/mcm$ space group) which possesses 2 cation sites in the TM layer (2*b* and 4*d*), was therefore used to fit the n-PDF data.[22] For $Na_{0.67}Fe_{0.25}Mn_{0.6}Mg_{0.15}O_2$, all of the Mg and most of the Fe occupy the 2*b* site of the honeycomb while for $Na_{0.67}Fe_{0.5}Mn_{0.5}O_2$, both 2*b* and 4*d* sites are occupied by both Fe and Mn (see Tables S1 and S2, Supporting Information), indicating the formation of a local honeycomb ordering in $Na_{0.67}Fe_{0.25}Mn_{0.6}Mg_{0.15}O_2$ over the medium range rather than a nanophase segregation between Fe/Mn-rich and Mg/Mn-rich domains.

Among the whole series of materials synthesized, $Na_{0.67}Fe_{0.25}Mn_{0.6}Mg_{0.15}O_2$, corresponding approximately to the middle of the $Na_{0.67}Mn_{0.72}Mg_{0.28}O_2$-$Na_{0.67}Fe_{0.5}Mn_{0.5}O_2$ tie-line, delivers the best electrochemical performance in terms of discharge voltage and capacity as well as cycling stability, as shown in Figure S4, Supporting Information. **Figure 2** represents the first charge/discharge cycle of $Na_{0.67}Fe_{0.5}Mn_{0.5}O_2$ and $Na_{0.67}Fe_{0.25}Mn_{0.6}Mg_{0.15}O_2$ materials as well as their capacity and voltage retention over 25 cycles. They exhibit comparable first charge curves with the presence of a high voltage plateau which differs in length, long for $Na_{0.67}Fe_{0.5}Mn_{0.5}O_2$ and shorter for $Na_{0.67}Fe_{0.25}Mn_{0.6}Mg_{0.15}O_2$. In the Mg-substituted material, the charge capacity up to the beginning of the high voltage plateau closely matches with the capacity expected for Mn^{3+}/Mn^{4+} and Fe^{3+}/Fe^{4+} redox. The ability to extract more charge than can be accounted for by cation redox is consistent with the presence of O-redox. In $Na_{0.67}Fe_{0.5}Mn_{0.5}O_2$, sodium extraction could in principle be fully charge-compensated by cationic redox, since the theoretical TM capacity exceeds the total capacity extracted

© 2022 The Authors. Advanced Energy Materials published by Wiley-VCH GmbH

16146840, 2022, 30, Downloaded from https://onlinelibrary.wiley.com/doi/10.1002/aenm.202200702 by Test, Wiley Online Library on [13/10/2022]. See the Terms and Conditions (https://onlinelibrary.wiley.com/terms-and-conditions) on Wiley Online Library for rules of use; OA articles are governed by the applicable Creative Commons License

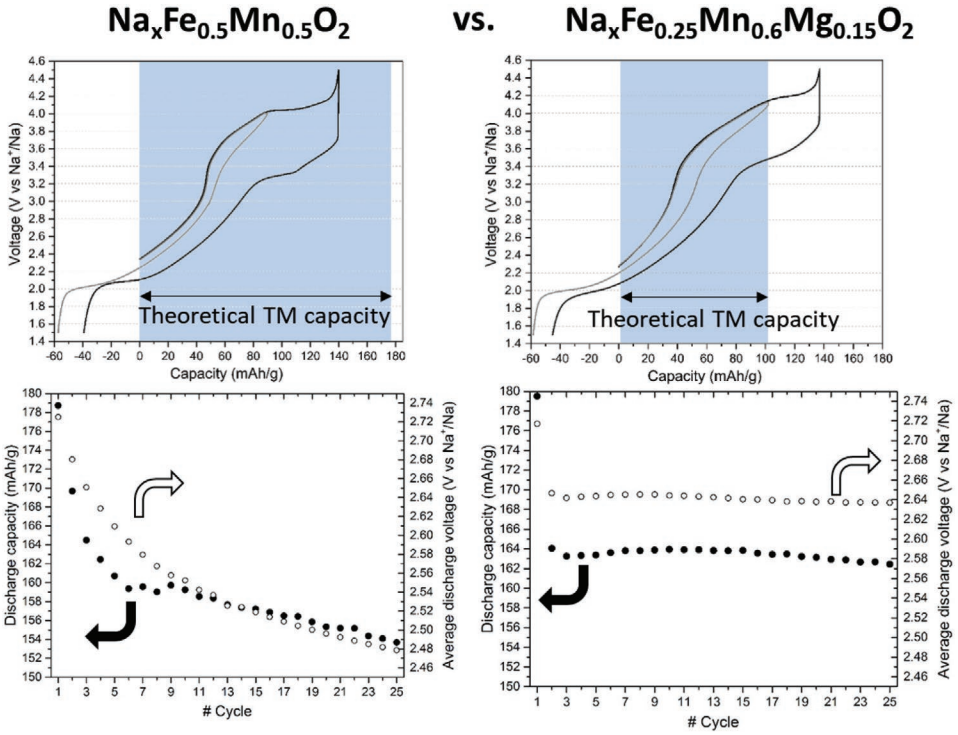


Figure 2. a) First charge-discharge cycle in the 1.5 – 4.5 V versus Na^+/Na range (black line) and until the beginning of the high voltage plateau (grey line). b) Voltage and capacity retention of $Na_{0.67}Fe_{0.5}Mn_{0.5}O_2$ (left) and $Na_{0.67}Fe_{0.25}Mn_{0.6}Mg_{0.15}O_2$ (right) over 25 cycles at a current density of 10 mA g^{-1}.

on charge, Figure 2. However, the observation for both materials that charging across the high voltage plateau introduces a significant voltage hysteresis is consistent with the presence of O-redox. Although both materials deliver similar first discharge capacities and average voltages, there is a marked difference in their behavior on cycling. $Na_{0.67}Fe_{0.5}Mn_{0.5}O_2$ exhibits continuous fading of capacity and discharge voltage, while stable capacity and voltage on cycling (≈163 mAh g^{-1} and 2.64 V) are observed for $Na_{0.67}Fe_{0.25}Mn_{0.6}Mg_{0.15}O_2$ up to 100 cycles (Figure S5, Supporting Information). In order to understand the role of Mg substitution in stabilizing the voltage and capacity on cycling, the redox mechanism, as well as the evolution of the local environments during cycling of both materials were investigated.

2.2. Cation Migration and Redox Mechanism

2.2.1. Mg-Substitution Promotes Complete $Fe^{3+/4+}$ Oxidation Before O-Redox

Operando Mn and Fe K-edge X-ray absorption near edge structure (XANES) as well as ex situ O K-edge soft X-ray absorption spectroscopy (sXAS) and O K-edge resonant inelastic X-ray scattering (RIXS) were employed to compare the redox mechanism in both materials during first charge/discharge cycle. As Fe is in the +3 oxidation state in both pristine materials, Mn is +3.67 and +3.8 respectively for $Na_{0.67}Fe_{0.5}Mn_{0.5}O_2$ and $Na_{0.67}Fe_{0.25}Mn_{0.6}Mg_{0.15}O_2$. The evolution of the edge position of the Mn and Fe K-edges along with the associated charge and discharge curves are shown in **Figure 3**, the XANES spectra are given in Figure S6, Supporting Information. While the transitions from one redox process to another are not always abrupt, the following trends can be established. In both materials, during the first part of the charge, the Mn K-edge shifts to higher energy (i.e., Mn redox), the charge passed is consistent with formation of Mn^{4+} and on further charging, the dominant change occurs in the Fe K-edge (i.e., Fe redox), Figure 3. The high voltage plateau is associated with oxygen redox, with the characteristic peaks appearing on the O K-edge sXAS (see Figure S7, Supporting Information) and RIXS spectra (denoted as A and B in Figure 3).[16] Note that the TM K-edges are sensitive to coordination environment as well as oxidation state and the small apparent changes in energy observed across the high voltage plateau are likely due to structural change associated with O-redox, rather than further Fe/Mn redox activity, as observed in other O-redox materials.[23] On discharge, the charge compensation mechanism is reversed with reduction of Fe^{4+} occurring predominantly first, as revealed by the shift of the Fe K-edge to lower energy, and the persistence of the O K-edge RIXS features until ≈3.3 V versus Na^+/Na. Oxygen and Mn are then reduced at higher sodium contents. This sequence change in the charge compensation mechanism is widely observed among O-redox materials as exemplified by $Li_{1.2}Ni_{0.13}Mn_{0.54}Co_{0.13}O_2$ in which O^{2-} oxidation on charge occurs at a higher voltage than subsequent O reduction on discharge due to structural change and O–O dimerization.[24,25]

Although both materials reveal similar trends during the first cycle, the amplitude of the Fe K-edge shift is significantly higher in the Mg-substituted material (1.45 eV vs. 0.55 eV). Mg

© 2022 The Authors. Advanced Energy Materials published by Wiley-VCH GmbH

16146840, 2022, 30, Downloaded from https://onlinelibrary.wiley.com/doi/10.1002/aenm.202200702 by Test, Wiley Online Library on [13/10/2022]. See the Terms and Conditions (https://onlinelibrary.wiley.com/terms-and-conditions) on Wiley Online Library for rules of use; OA articles are governed by the applicable Creative Commons License

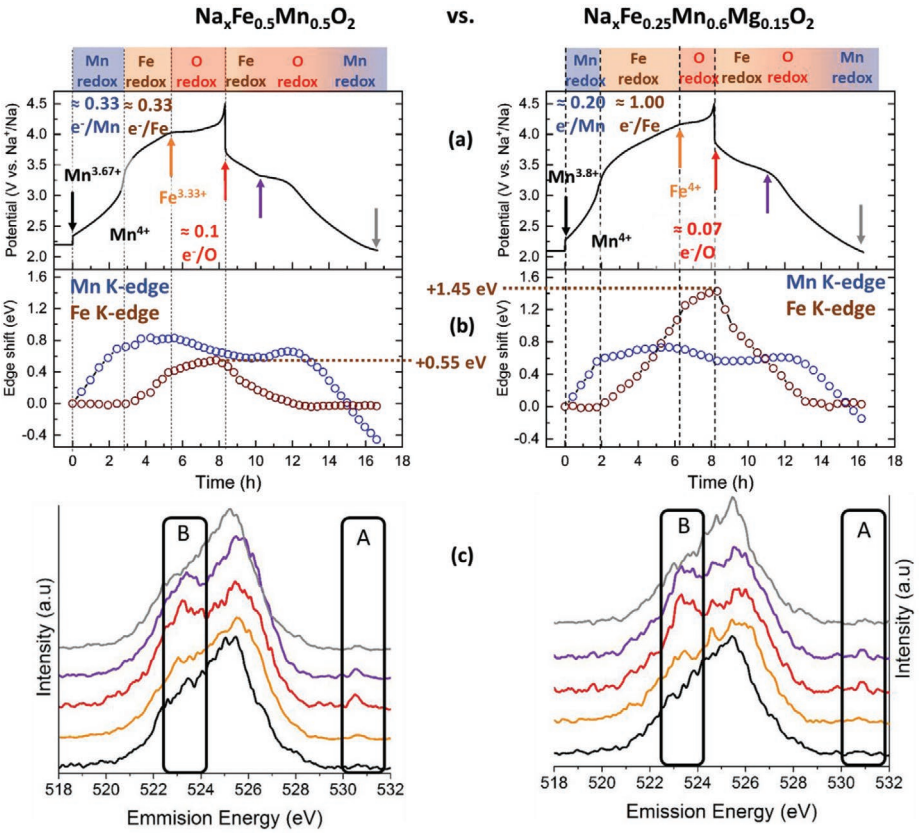


Figure 3. a) Galvanostatic curves of $Na_{0.67}Fe_{0.5}Mn_{0.5}O_2$ (left panel) and $Na_{0.67}Fe_{0.25}Mn_{0.6}Mg_{0.15}O_2$ (right panel) along with b) the evolution of the Fe (brown circles) and Mn (blue circles) K-edge energy position is taken at half height of edge jump. The corresponding Fe K-edge XANES spectra are displayed in Figure S5, Supporting Information. c) ex situ O K-edge RIXS spectra were collected at an excitation energy of 531 eV. The elastic peak (A) and the energy loss peak at 8 eV (B) associated to oxidized oxides appear between 4.0 and 4.5 V on charge and disappear between 3.3 and 2.1 V upon discharge in both materials.

substitution promotes Fe-redox to a greater extent compared with that observed in $Na_{0.67}Fe_{0.5}Mn_{0.5}O_2$, where O-redox starts at a formal Fe oxidation state of $\approx Fe^{3.3+}$, whereas it closely matches with Fe^{4+} in $Na_{0.67}Fe_{0.25}Mn_{0.6}Mg_{0.15}O_2$. This result, although surprising, aligns with the ^{57}Fe Mossbauer results published previously, where Nazar and coworkers estimated the amount of Fe^{4+} at the end of the charge of $Na_{0.67}Fe_{0.5}Mn_{0.5}O_2$ at 32.5%.[6] Moreover, the charge passed before the beginning of the high voltage plateau associated with the P2/O2-like phase transition, in $Na_{0.67}Fe_{0.5}Mn_{0.5}O_2$, closely matches Fe in a +3.3 oxidation state.

2.2.2. Na Content Determines the Transition from Fe-Redox to O-Redox

An important and longstanding question in Fe-containing Na-ion transition metal oxide cathodes is what determines the degree to which Fe^{3+} can be oxidized to Fe^{4+} before O^{2-} oxidation sets in. Poor cycling stability of Fe-redox cathodes has been previously linked to a tendency of Fe to migrate in the structure,[6,8,26] however, looking at $Na_{0.67}Fe_{0.25}Mn_{0.6}Mg_{0.15}O_2$ in our study, it is possible to oxidize Fe^{3+} completely to Fe^{4+} before the high voltage O-redox plateau in the Mg substituted sample, questioning whether Fe migration is an inevitable consequence of Fe redox.

In order to probe transition metal migration in both compounds, Mn, Fe, and Mg K-edge EXAFS, **Figure 4**, were collected on charge. In the Mg-substituted material, $Na_{0.67}Fe_{0.25}Mn_{0.6}Mg_{0.15}O_2$, at the end of charge, Fe K-edge EXAFS shows no significant change compared with the pristine material, except a shortening of the Fe–O and Fe–M bonds as well as a slight decrease in the 2nd shell intensity associated with the creation of Na vacancies in the AM layer. In contrast, a clear decrease in the 2nd shell intensity at the Mn K-edge is observed. As Mg^{2+} is located principally around Mn (and not Fe) due to the local honeycomb ordering in this material (see Figure 1), the changes in the Mn and Fe 2nd shells are in accord with Mg^{2+} migration from the TM layer to the AM layer giving rise to vacancies around Mn in the TM layer. This is supported by the Mg K-edge EXAFS data in Figure 4, which shows significant changes in the first coordination sphere with the appearance of a new feature at low radial distance, corresponding to the Mg–O bond length expected for Mg^{2+} in a tetrahedral site, as observed for the charged state of P2-$Na_{0.67}Mn_{0.72}Mg_{0.28}O_2$.[27] The fit of the Mg K-edge EXAFS data, shown in Figure S8 and summarized in Table S4, Supporting Information, reveals a similar behavior in $Na_{0.67}Fe_{0.25}Mn_{0.6}Mg_{0.15}O_2$ were about. 50% of the Mg is displaced into tetrahedral and octahedral sites in the AM layer. For $Na_{0.67}Fe_{0.5}Mn_{0.5}O_2$, the changes in the

© 2022 The Authors. Advanced Energy Materials published by Wiley-VCH GmbH

16146840, 2022, 30, Downloaded from https://onlinelibrary.wiley.com/doi/10.1002/aenm.202200702 by Test, Wiley Online Library on [13/10/2022]. See the Terms and Conditions (https://onlinelibrary.wiley.com/terms-and-conditions) on Wiley Online Library for rules of use; OA articles are governed by the applicable Creative Commons License

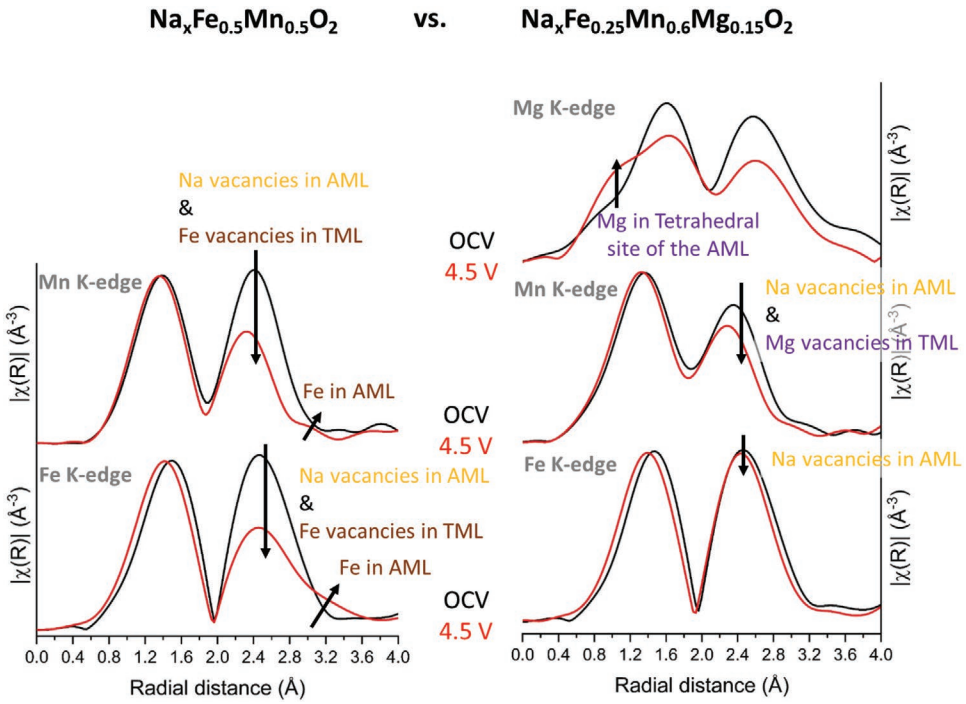


Figure 4. Ex situ Fe, Mn and Mg K-edge EXAFS spectra collected at open-circuit voltage, OCV (black) and 4.5 V (red) for $Na_{0.67}Fe_{0.5}Mn_{0.5}O_2$ (left) and $Na_{0.67}Fe_{0.25}Mn_{0.6}Mg_{0.15}O_2$ (right).

EXAFS are different. The decrease in 2nd shell intensity signals the creation of vacancies in the TM layer around Fe and Mn (which are disordered in the TM layer) and the presence of a shoulder at a longer radial distance (≈3–3.2 Å) is consistent with the TM ions in the AM layer. The greater intensity of this shoulder in the case of the Fe K-edge EXAFS suggests that it is Fe that is displaced to the AM layer. As illustrated in Figure S9, Supporting Information, a TM cation residing in the AM layer stacked as an O2-type sequence is surrounded by 9 TM located in the adjacent TM layers (at ≈3.3–3.4 Å) while each of the 6 TM ions next to the vacancy left in the TM layer are surrounded by 5 TM within the TM layer (at ≈2.9–3.1 Å) and only 1 TM in the AM layer (at ≈3.2–3.4 Å). It is important to note that both materials in the charged state exhibit very similar average Fe–O bond lengths, despite Fe being significantly more oxidized in charged $Na_{0.67}Fe_{0.25}Mn_{0.6}M_{0.15}O_2$ (Fe^{4+}) than $Na_{0.67}Fe_{0.5}Mn_{0.5}O_2$ ($Fe^{3.3+}$). The short Fe^{3+}-O bond indicates the presence of Fe^{3+} in tetrahedral sites of the Na layer in charged $Na_{0.67}Fe_{0.5}Mn_{0.5}O_2$. By comparison with known compounds, the average Fe-O bond length in β-$NaFeO_2$ (tetrahedral Fe^{3+}, d(Fe–O) = 1.93 Å)[28] is similar to that observed in the perovskite $CaFeO_3$ (octahedral Fe^{4+}, d(Fe–O) = 1.92 Å)[29] but is much shorter than for α-$NaFeO_2$ (octahedral Fe^{3+}, (Fe–O) = 2.05 Å)[30] This aligns a previous report by Nazar and co-workers that 17% of the Fe in charged $Na_{0.67}Fe_{0.5}Mn_{0.5}O_2$ is found as tetrahedral Fe^{3+} from ^{57}Fe Mössbauer.[6] The fitting of Fe K-edge EXAFS spectrum of charged $Na_{0.67}Fe_{0.5}Mn_{0.5}O_2$, provided in Figure S8, Supporting Information, and summarized in Table S3, Supporting Information, matches well with this model.

Activation of O-redox occurs in layered compounds which possess A–O–A dumbbells (with A = alkali,[31,32] alkali-earth,[16] Zn^{2+} [33] or vacancies[34]). The weak A-O2p-A interactions raise the energy of the O2p states making them accessible for oxidation at lower potentials.[35] In stoichiometric materials with a fully dense TM layer, such as $Na_{0.67}[Fe_{0.5}Mn_{0.5}]O_2$, O-redox can only be brought into the voltage range of $Fe^{3+/4+}$ redox when transition metal ions can migrate, forming □-O-□ configurations. In P-type layered cathodes, out-of-plane migration is only permitted when, at sufficiently high levels of desodiation, the layer stacking changes to adopt O-type stacking, forming octahedral sites in the Na layer. In both $Na_{0.67}Fe_{0.5}Mn_{0.5}O_2$ and $Na_{0.67}Fe_{0.25}Mn_{0.6}Mg_{0.15}O_2$, this transition from P-type to O-type stacking (O2-like and OP4-like stackings respectively, see Figure S10, Supporting Information), occurs at a similar Na content of 0.3 in both cases (0.33 and 0.3, respectively), driven by electrostatic interactions between oxide ions in adjacent layers. In the case of $Na_{0.67}[Fe_{0.5}Mn_{0.5}]O_2$, following full oxidation of Mn to +4, the oxidation of Fe only reaches $Fe^{3.3+}$ before the Na content depletes to 0.3. Beyond this, the un-oxidized Fe^{3+} migrates to octahedral sites in the Na layer, bringing the O-redox into the accessible voltage range and triggering the switch from Fe-redox to O-redox. In contrast, in $Na_{0.67}Fe_{0.25}Mn_{0.6}Mg_{0.15}O_2$, Fe^{3+} can be fully oxidized to Fe^{4+} before a Na content of 0.3 is reached. Upon further desodiation, Mg^{2+} migrates to the Na layer instead of Fe^{4+}, which remains in the TM layer, **Figure 5**. This shift from Fe migration to Mg migration also has important implications for capacity and voltage fade arising from the Fe-redox process.

2.2.3. Origin of the Voltage Fade

The discharge profile for $Na_{0.67}Fe_{0.25}Mn_{0.6}Mg_{0.15}O_2$ is relatively invariant on cycling, in contrast to that for $Na_{0.67}Fe_{0.5}Mn_{0.5}O_2$,

© 2022 The Authors. Advanced Energy Materials published by Wiley-VCH GmbH

16146840, 2022, 30, Downloaded from https://onlinelibrary.wiley.com/doi/10.1002/aenm.202200702 by Test, Wiley Online Library on [13/10/2022]. See the Terms and Conditions (https://onlinelibrary.wiley.com/terms-and-conditions) on Wiley Online Library for rules of use; OA articles are governed by the applicable Creative Commons License

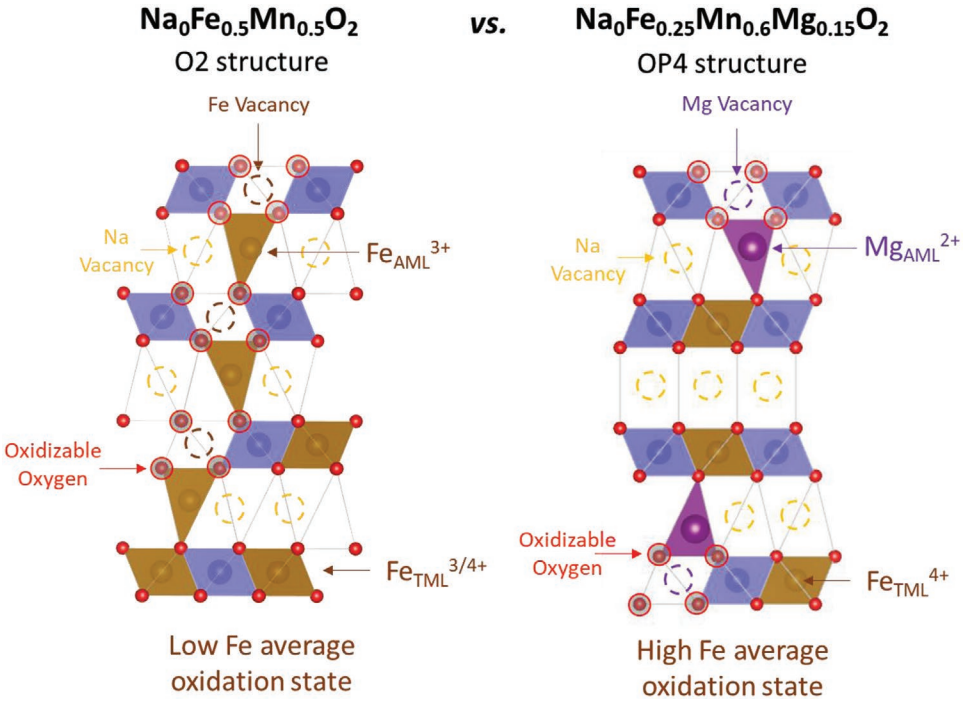


Figure 5. Structure of $Na_0Fe_{0.5}Mn_{0.5}O_2$ (left) and $Na_0Fe_{0.25}Mn_{0.6}Mg_{0.15}O_2$ (right), the out-of-plane migration of cations generates □-O-□ dumbbells in which O^{2-} ions can then be oxidized.

for which the voltage drops significantly, see **Figure 6**a. Note that, for that latter, after 25 cycles, the average discharge voltage approximately matches that observed for $Na_{0.67}Mn_{0.72}Mg_{0.28}O_2$, a pure Mn/O redox material. In order to understand this voltage fade, ex situ Fe K-edge XANES data were collected at the 1st and 25th charged and discharged states for each material (Figure 6b). In $Na_{0.67}Fe_{0.5}Mn_{0.5}O_2$, for which the high voltage is lost over cycling, the shift of the Fe K-edge on 25th charge is very small (0.15 eV) indicating that Fe redox is almost no longer active. In contrast, a significant Fe K-edge energy shift is still observed on the 25th charge of $Na_{0.67}Fe_{0.25}Mn_{0.6}Mg_{0.15}O_2$ (1.10 eV) which retains the high voltage feature associated with Fe-redox on the following discharge. These results suggest a correlation between the voltage fade and loss of Fe redox activity.

To understand this Fe redox decay, ex situ EXAFS and NPD data were collected. For $Na_{0.67}Fe_{0.5}Mn_{0.5}O_2$, on reinsertion of Na after the 1st charge, the Fe migration on charging appears to be only partially reversible as evidenced by NPD revealing the persistence of 0.027(4) Fe in the AM layer at the first discharge, Figure S11 and Table S5, Supporting Information, in good agreement with STEM observations on others Fe containing layered oxides.[26] These Fe most likely reside in local stacking faults of O2-type layer stacking in the otherwise predominantly P2-type discharged structure. The EXAFS data in **Figure 7** show a decrease of the 2nd shell intensity indicating increase in cation vacancies in the TM layer, coupled with the increase in intensity of the shoulder in the Fe K-edge EXAFS which indicates increasing occupancy of Fe in the AM layer. These changes grow on cycling, i.e., there is a net accumulation of Fe in the AM layers. Therefore, fewer and fewer Fe ions are oxidized over extended cycling. The loss of high voltage $Fe^{3+/4+}$ redox capacity is partially compensated by a small amount of low voltage $Mn^{3+/4+}$ reduction on discharge as evidenced by a further shift to lower energy of the Mn K-edge from XANES (see Figure S12, Supporting Information), leading overall to voltage and capacity fade. NPD data taken at 1st discharge of $Na_{0.67}Fe_{0.25}Mn_{0.6}Mg_{0.15}O_2$ (Figure S11 and Table S6, Supporting Information) reveal that the migration of Mg back into the TM layer appears to be mostly reversible (0.008(3) Mg remain in the AM layer in the discharged $Na_{0.67}Fe_{0.25}Mn_{0.6}Mg_{0.15}O_2$ versus 0.027(4) Fe in $Na_{0.67}Fe_{0.5}Mn_{0.5}O_2$). After extensive cycling, the 2nd shell intensity at Fe and Mn K-edge tends to equalize indicating that the local honeycomb arrangement of Mn around Fe and Mg is lost but the redox mechanism remains similar to that on the 1st cycle (see Figure S11, Supporting Information) with retention of high voltage and capacity.

The data we present here for $Na_{0.67}Fe_{0.5}Mn_{0.5}O_2$ and $Na_{0.67}Fe_{0.25}Mn_{0.6}Mg_{0.15}O_2$ show that they both exhibit out-of-plane metal migration. However, crucially, the identity of the migrating metal is different in each case. For $Na_{0.67}Fe_{0.5}Mn_{0.5}O_2$, it is Fe that migrates to the AM layer. In such a P2-type material, this Fe migration is allowed by the TM layers gliding at high voltage providing suitable sites for Fe in the AM layer. Therefore, the onset of O-redox (i.e., end of Fe-redox) is accompanied with a P2 to O2-type phase transition. The out-of-plane Fe migration in $Na_{0.67}Fe_{0.5}Mn_{0.5}O_2$ is only partially reversible on discharge and Fe redox activity is rapidly lost during the 25 first cycles. Fe being reduced at higher voltage than O and Mn upon discharge, this Fe redox decay explains the rapid voltage fade observed for $Na_{0.67}Fe_{0.5}Mn_{0.5}O_2$ while the Mn over-reduction only partially compensate the Fe redox capacity fade, leading to a net capacity loss. In contrast, upon discharge of $Na_{0.67}Fe_{0.25}Mn_{0.6}Mg_{0.15}O_2$, Mg more

© 2022 The Authors. Advanced Energy Materials published by Wiley-VCH GmbH

16146840, 2022, 30, Downloaded from https://onlinelibrary.wiley.com/doi/10.1002/aenm.202200702 by Test, Wiley Online Library on [13/10/2022]. See the Terms and Conditions (https://onlinelibrary.wiley.com/terms-and-conditions) on Wiley Online Library for rules of use; OA articles are governed by the applicable Creative Commons License

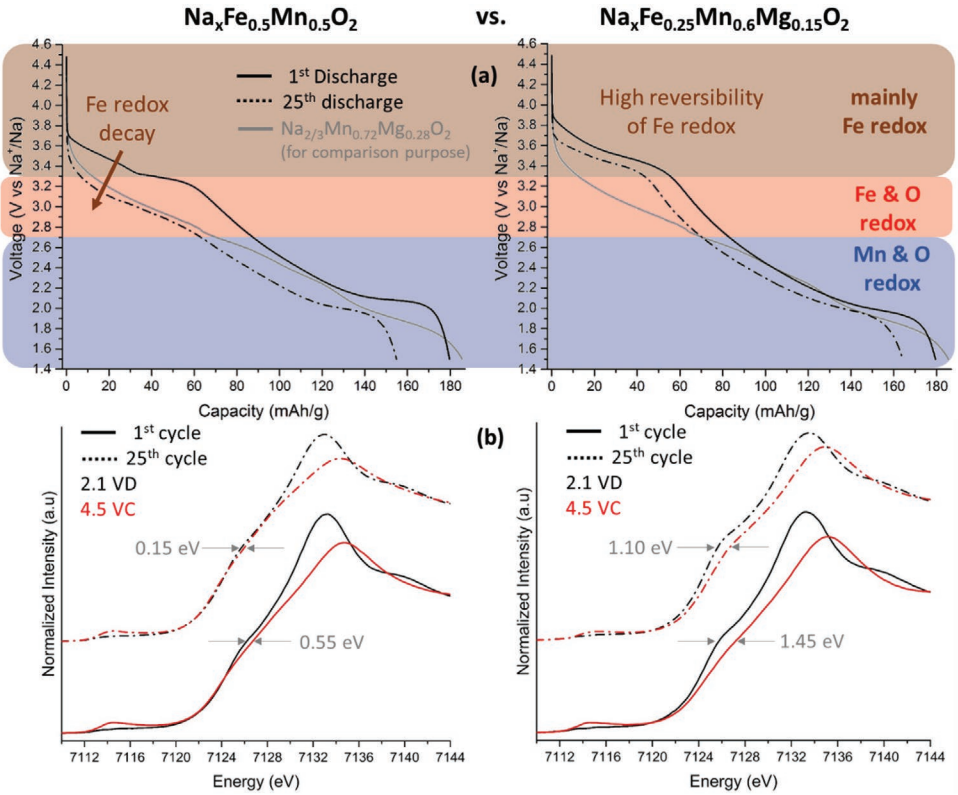


Figure 6. (a) 1st and 25th discharge profile of $Na_{0.67}Fe_{0.5}Mn_{0.5}O_2$ (left) and $Na_{0.67}Fe_{0.25}Mn_{0.6}Mg_{0.15}O_2$ (right), the first discharge of $Na_{0.67}Mn_{0.72}Mg_{0.28}O_2$ is shown for comparison with a pure O/Mn redox material. The approximate voltage ranges of Fe, Mn, and O reduction are extrapolated from that obtained with operando XANES and ex situ RIXS shown in Figure 3. b) ex-situ Fe K edge XANES collected at 4.5 V (red) and 2.1 V (black) during 1st (solid line) and 25th (dashed line) cycle of $Na_{0.67}Fe_{0.5}Mn_{0.5}O_2$ (left) and $Na_{0.67}Fe_{0.25}Mn_{0.6}Mg_{0.15}O_2$ (right).

reversibly migrates back to the TM layer, the pristine structure is mostly recovered, and the Fe redox activity is mostly preserved upon subsequent cycles leading to an excellent cycling stability. Consequently, this new earth abundant and cost-effective material delivers a state-of-the-art energy density of ≈430 Wh kg^{-1} in half cell configuration versus Na after 100 cycles (against ≈340 Wh kg^{-1} for $Na_{0.67}Fe_{0.5}Mn_{0.5}O_2$).

3. Conclusion

By substituting Mg into $Na_{0.67}Fe_{0.5}Mn_{0.5}O_2$, full utilization of the Fe^{3+}/Fe^{4+} redox couple can be achieved without substantial voltage fade or capacity loss. On charging $Na_{0.67}Fe_{0.5}Mn_{0.5}O_2$, Fe oxidation only reaches $Fe^{3.3+}$ before the Na content is sufficiently depleted to trigger the transition from P-type to O-type stacking. O-type stacking permits the migration of Fe^{3+} to the Na layer, forming □-O-□ configurations which trigger O-oxidation at a lower potential than further Fe oxidation. This out-of-plane Fe migration is not completely reversible and the Fe-redox activity continuously decreases, leading to voltage fade and capacity loss. In Mg substituted $Na_{0.67}Fe_{0.25}Mn_{0.6}Mg_{0.15}O_2$, Fe can be fully oxidized to +4 before Na content reaches 0.3. Further desodiation results in O-redox and migration of Mg^{2+} to the Na layer instead of Fe^{4+}. This Mg out-of-plane migration being essentially reversible upon discharge, the long-term reversibility of the Fe^{3+}/Fe^{4+} redox couple is realized leading to an improved voltage and capacity retention on cycling. This finding opens the way toward high-performance, earth-abundant layered sodium TM oxide cathodes for Na-ion batteries.

4. Experimental Section

Synthesis: The $Na_{0.67}Mg_xMn_yFe_zO_2$ materials were synthesized by a solid-state reaction between stoichiometric amounts of Na_2CO_3 (≥99.0%, Aldrich), MgO (≥99.99%, Aldrich), and Mn_2O_3 (≥99.9%, Aldrich) and Fe_2O_3 (≥99.9%, Aldrich). The precursors were ball-milled for 30 minutes at a rotation rate of 350 revolutions per minute in a Retsch PM100 planetary ball-mill. This mixture was then heated at 950 °C for 10 h under Air and cooled to room temperature. In order to remove the surface carbonates, the powder was reground prior to a second heating step at 700 °C under an Ar atmosphere at 10 °C min^{-1} and then immediately cooled to room temperature by moving the sample out of the heating zone. The material was transferred to an Ar-filled glove-box and stored under Ar without any exposure to air.

Electrochemistry Test: Electrodes were prepared by mixing 80 wt% active material, 10 wt% acetylene carbon black, and 10 wt% polytetrafluoroethylene (PTFE) binder (in a mortar pestle and rolling out thin free-standing films of the mixture). Electrochemical testing was carried with Na metal-disk as anode and a 1M $NaPF_6$ dissolved in EC:DEC solution electrolyte. Galvanostatic charge-discharge was carried out in coin cells using a Maccor Series 4000 at a rate of 10 mAg^{-1}.

Diffraction: Synchrotron X-ray powder diffraction (XRPD) was collected on 11-BM (APS, USA) in 0.5 mm kapton capillary for 1h at 30 keV. Neutron scattering was carried out on the POLARIS diffractometer (ISIS, UK) in time-of-flight mode in cylindrical 6 mm-diameter vanadium cans and measured for 7 h on ≈1 g of powder. The cycled samples have been

© 2022 The Authors. Advanced Energy Materials published by Wiley-VCH GmbH

16146840, 2022, 30, Downloaded from https://onlinelibrary.wiley.com/doi/10.1002/aenm.202200702 by Test, Wiley Online Library on [13/10/2022]. See the Terms and Conditions (https://onlinelibrary.wiley.com/terms-and-conditions) on Wiley Online Library for rules of use; OA articles are governed by the applicable Creative Commons License

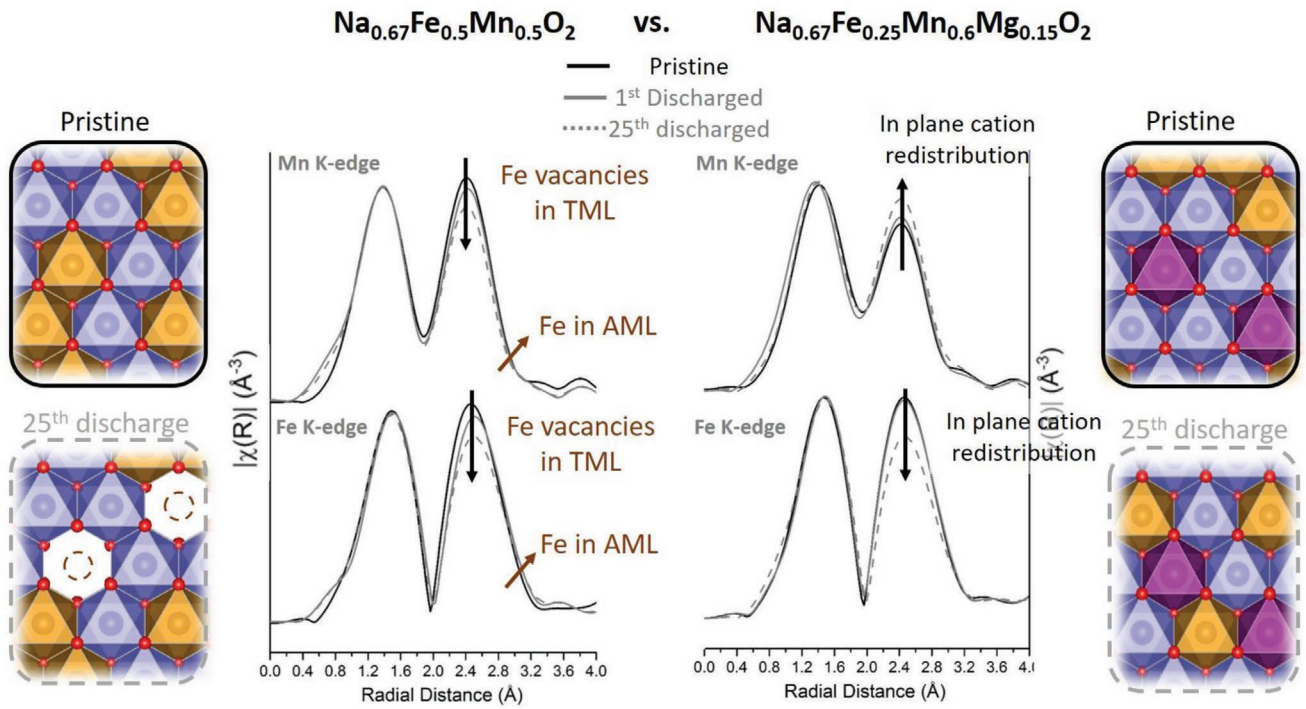


Figure 7. Ex situ Mn and Fe K-edge EXAFS at OCV (black) and 2.1 V (grey) at the 1st (solid line) and 25th discharge (dashed line) for $Na_{0.67}Fe_{0.5}Mn_{0.5}O_2$ (left) and $Na_{0.67}Fe_{0.25}Mn_{0.6}Mg_{0.15}O_2$ (right).

prepared in similar way than described above but in a 10 cm diameter in-house constructed cell and replacing the binder with additional carbon. Rietveld analysis of XRPD and Neutron Powder Diffraction (NPD) were carried out using the Fullprof software package.[36] The total scattering data have been extracted from ND after correction for the effects of background scattering from the sample environment and beam attenuation using the program GudrunN.[36] The resultant normalized total scattering structure factors were Fourier transformed to obtain the corresponding total radial pair distribution functions (n-PDF) which were analyzed using PDF-GUI.[37]

Operando and Ex Situ X-ray absorption spectroscopy (XAS): TM K-edge X-ray absorption near edge structure (XANES) and extended X-ray absorption fine structure (EXAFS) data were collected on B18 Core EXAFS beamline at diamond light source (DLS, UK). Absorption spectra of Mn and Fe K-edge were collected in transmission mode using a Si (111) double crystal monochromator. Ionization chambers were utilized to measure the intensity of the incident and transmitted X-ray beam whose the energy have been calibrated using Mn or Fe reference foil spectra. Operando data have been collected in a homemade cell, on active materials/PTFE/C (80/10/10) electrodes cycled at a rate of 15 mA g^{-1}. Ex situ samples have been prepared as described in the electrochemical test section, the electrodes were then washed in DMC several times and dried under vacuum at room temperature for 5 min prior to the measurement. Each spectrum were summed over 3 scans, calibrated, background subtracted, normalized and then the k^2-weighted EXAFS data have been extracted using the ≈2.5–9.0 $Å^{-1}$ k-range with the Athena software.[38] The intensity of all EXAFS spectra shown in this article have been normalized over the first shell intensity.

Ex Situ Soft X-Ray Absorption Spectroscopy (sXAS) and Resonant Inelastic X-Ray Scattering (RIXS): Ex situ Mg K-edge sXAS and O K-edge RIXS data were collected on BL27SU (Spring8, Japan). Ex situ cathode samples were loaded onto adhesive copper tape and measured under 10^{-6} Pa high-vacuum conditions. To obtain sXAS spectra at the Mg K-edge, the partial fluorescence yield (PFY) signal was recorded in 1200–1700 eV energy range and the k^2-weighted EXAFS spectra have then been extracted using Athena.[38] The O K-edge RIXS spectra were recorded using an XES monochromator and a CCD detector with a resolution of 0.5 eV in the energy range of interest.

Supporting Information

Supporting Information is available from the Wiley Online Library or from the author.

Acknowledgements

P.G.B. is indebted to the EPSRC, the Henry Royce Institute for Advanced Materials (EP/R00661X/1, EP/S019367/1, EP/R010145/1), the Faraday Institution (FIRG007, FIRG008) as well as Shell for financial support and especially Dr. Peter A.A. Klusener (Senior process development chemist, Shell) and Dr James W. Somerville for fruitful discussions. The authors acknowledge technical and experimental support at the B18 (DLS, UK) by Gianntonnio Cibin, at BL27SU (Spring8, Japan) by Dr. Kazuki Tsuruta, by Dr. Helen Playford and Dr. Ron Smith at POLARIS (ISIS, UK). They also thank 11-BM mail service staff (APS, USA) for SXRD data.

Conflict of Interest

The authors declare no conflict of interest.

Data Availability Statement

The data that support the findings of this study are available from the corresponding author upon reasonable request.

Keywords

Na-ion batteries, cathodes, iron redox, oxygen redox

Received: February 28, 2022
Revised: May 26, 2022
Published online: June 26, 2022

© 2022 The Authors. Advanced Energy Materials published by Wiley-VCH GmbH

16146840, 2022, 30, Downloaded from https://onlinelibrary.wiley.com/doi/10.1002/aenm.202200702 by Test, Wiley Online Library on [13/10/2022]. See the Terms and Conditions (https://onlinelibrary.wiley.com/terms-and-conditions) on Wiley Online Library for rules of use; OA articles are governed by the applicable Creative Commons License

[1] C. Vaalma, D. Buchholz, M. Weil, S. Passerini, *Nat. Rev. Mater.* **2018**, *3*, 18013.
[2] N. Yabuuchi, K. Kubota, M. Dahbi, S. Komaba, *Chem. Rev.* **2014**, *114*, 11636.
[3] K. Kubota, S. Kumakura, Y. Yoda, K. Kuroki, S. Komaba, *Adv. Energy Mater.* **2018**, *8*, 1703415.
[4] M. Chen, Q. Liu, S. W. Wang, E. Wang, X. Guo, S. L. Chou, *Adv. Energy Mater.* **2019**, *9*, 1803609.
[5] N. Yabuuchi, M. Kajiyama, J. Iwatate, H. Nishikawa, S. Hitomi, R. Okuyama, R. Usui, Y. Yamada, S. Komaba, *Nat. Mater.* **2012**, *11*, 512.
[6] E. Talaie, V. Duffort, H. L. Smith, B. Fultz, L. F. Nazar, *Energy Environ. Sci.* **2015**, *8*, 2512.
[7] B. M. De Boisse, D. Carlier, M. Guignard, L. Bourgeois, C. Delmas, *Inorg. Chem.* **2014**, *53*, 11197.
[8] Y. Li, Y. Gao, X. Wang, X. Shen, Q. Kong, R. Yu, G. Lu, Z. Wang, L. Chen, *Nano Energy* **2018**, *47*, 519.
[9] J. W. Somerville, R. A. House, N. Tapia-Ruiz, A. Sobkowiak, S. Ramos, A. V. Chadwick, M. R. Roberts, U. Maitra, P. G. Bruce, *J. Mater. Chem. A* **2018**, *6*, 5271.
[10] J. S. Thorne, R. A. Dunlap, M. N. Obrovac, *J. Electrochem. Soc.* **2014**, *161*, A2232.
[11] E. Talaie, S. Y. Kim, N. Chen, L. F. Nazar, *Chem. Mater.* **2017**, *29*, 6684.
[12] J. Xu, D. H. Lee, R. J. Clément, X. Yu, M. Leskes, A. J. Pell, G. Pintacuda, X. Q. Yang, C. P. Grey, Y. S. Meng, *Chem. Mater.* **2014**, *26*, 1260.
[13] G. Singh, N. Tapia-Ruiz, J. M. L. del Amo, U. Maitra, J. W. Somerville, A. R. Armstrong, J. M. De Martinez de Ilarduya, T. Rojo, P. G. Bruce, *Chem. Mater.* **2016**, *28*, 5087.
[14] S. M. Oh, S. T. Myung, J. Y. Hwang, B. Scrosati, K. Amine, Y. K. Sun, *Chem. Mater.* **2014**, *26*, 6165.
[15] J. Billaud, G. Singh, A. R. Armstrong, E. Gonzalo, V. Roddatis, M. Armand, T. Rojo, P. G. Bruce, *Energy Environ. Sci.* **2014**, *7*, 1387.
[16] U. Maitra, R. A. House, J. W. Somerville, N. Tapia-Ruiz, J. G. Lozano, M. A. Pérez-Osorio, F. Massel, N. Guerrini, R. Hao, K. Luo, L. Jin, D. E. McNally, A. V. Chadwick, D. M. Pickup, S. Ramos, X. Lu, L. C. Duda, M. R. Roberts, P. G. Bruce, *Nat. Chem.* **2018**, *10*, 288.
[17] B. Song, E. Hu, J. Liu, Y. Zhang, X. Q. Yang, J. Nanda, A. Huq, K. Page, *J. Mater. Chem. A* **2019**, *7*, 1491.
[18] K. Du, J. Zhu, G. Hu, H. Gao, Y. Li, J. B. Goodenough, *Energy Environ. Sci.* **2016**, *9*, 2575.
[19] N. Yabuuchi, R. Hara, M. Kajiyama, K. Kubota, T. Ishigaki, A. Hoshikawa, S. Komaba, *Adv. Energy Mater.* **2014**, *4*, 1301453.
[20] J. Jin, Y. Liu, X. Pang, Y. Wang, X. Xing, J. A. Chen, *Sci. China Chem.* **2021**, *64*, 385.
[21] P. Strobel, B. Lambert-Andron, *J. Solid State Chem.* **1988**, *75*, 90.
[22] N. Yabuuchi, R. Hara, K. Kubota, J. Paulsen, S. Kumakura, S. Komaba, *J. Mater. Chem. A* **2014**, *2*, 16851.
[23] H. Koga, L. Croguennec, M. Ménétrier, P. Mannessiez, F. Weill, C. Delmas, S. Belin, *J. Phys. Chem. C* **2014**, *118*, 11, 5700.
[24] G. Assat, D. Foix, C. Delacourt, A. Iadecola, R. Dedryvère, J.-M. Tarascon, *Nat. Commun.* **2017**, *8*, 2219.
[25] R. A. House, G. J. Rees, M. A. Pérez-Osorio, J. J. Marie, E. Boivin, A. W. Robertson, A. Nag, M. Garcia-Fernandez, K. J. Zhou, P. G. Bruce, *Nat. Energy* **2020**, *5*, 777.
[26] X. Li, Y. Wang, D. Wu, L. Liu, S. H. Bo, G. Ceder, *Chem. Mater.* **2016**, *28*, 6575.
[27] E. Boivin, R. A. House, M. A. Pérez-Osorio, J. J. Marie, U. Maitra, G. Rees, P. G. Bruce, *Joule* **2021**, *5*, 1267.
[28] F. Bertaut, P. Blim, *C. R. Hebd. Seances Acad. Sci.* **1954**, *239*, 429.
[29] T. Takeda, R. Kanno, Y. Kawamoto, M. Takano, S. Kawasaki, T. Kamiyama, F. Izumi, *Solid State Sci.* **2000**, *2*, 673.
[30] Z. Tomkowicz, B. Van Laar, *Phys. Status Solidi A* **1974**, *26*, 683.
[31] K. Luo, M. R. Roberts, R. Hao, N. Guerrini, D. M. Pickup, Y. S. Liu, K. Edström, J. Guo, A. V. Chadwick, L. C. Duda, P. G. Bruce, *Nat. Chem.* **2016**, *8*, 684.
[32] B. M. De Boisse, G. Liu, J. Ma, S. I. Nishimura, S. C. Chung, H. Kiuchi, Y. Harada, J. Kikkawa, Y. Kobayashi, M. Okubo, A. Yamada, *Nat. Commun.* **2016**, *7*, 11397.
[33] X. Bai, M. Sathiya, B. Mendoza-Sánchez, A. Iadecola, J. Vergnet, R. Dedryvère, M. Saubanère, A. M. Abakumov, P. Rozier, J. M. Tarascon, *Adv. Energy Mater.* **2018**, *8*, 1802379.
[34] B. M. De Boisse, S. Nishimura, E. Watanabe, L. Lander, A. Tsuchimoto, J. Kikkawa, E. Kobayashi, D. Asakura, M. Okubo, A. Yamada, *Adv. Energy Mater.* **2018**, *8*, 1800409.
[35] D. H. Seo, J. Lee, A. Urban, R. Malik, S. Kang, G. Ceder, *Mater. Nat. Chem.* **2016**, *8*, 692.
[36] J. Rodriguez-carvajal, *Phys. B* **1993**, *192*, 55.
[37] P. Juhás, J. N. Louwen, L. van Eijck, E. T. C. Vogt, S. J. L. Billinge, *J. Appl. Crystallogr.* **2018**, *51*, 1492.
[38] B. Ravel, M. Newville, *J. Synchrotron Radiat.* **2005**, *12*, 537.

© 2022 The Authors. Advanced Energy Materials published by Wiley-VCH GmbH

16146840, 2022, 30, Downloaded from https://onlinelibrary.wiley.com/doi/10.1002/aenm.202200702 by Test, Wiley Online Library on [13/10/2022]. See the Terms and Conditions (https://onlinelibrary.wiley.com/terms-and-conditions) on Wiley Online Library for rules of use; OA articles are governed by the applicable Creative Commons License